# Formation of ice bands by winds

Ayumi Fujisaki[1,2,3] and Lie-Yauw Oey[2]

Received 14 September 2010; revised 23 May 2011; accepted 19 July 2011; published 15 October 2011.

[1] A mechanism for the formation of ice bands is proposed as a coupled response of ice edge and lee waves to wind under the hydrostatic approximation. A high-resolution ice-ocean coupled model is used in an $x$-$z$ domain with grid sizes $(x, z) = (250\ \text{m}, 1\ \text{m})$. Under an along-ice-edge wind, such that the Ekman transport is away from the ice edge, the nearly discontinuous surface stress between the ice-covered and open seas generates lee waves. A thin layer of high-potential vorticity fluid under the ice is produced by the Ekman forcing, enabling the ice edge to rapidly slip over less stratified water. This is favorable for supercritical conditions when lee waves are generated. Ice bands are formed by the corresponding convergences and divergences. The flow becomes subcritical farther behind the ice-edge but secondary lee waves and ice bands form because of the secondary stress discontinuity behind the lead ice band. An analytical solution is derived to show that ice bands have longer widths than the lee-wavelengths because the ice-ocean stress creates the smoothing effect. Vertical motions associated with the lee waves have speed of the order of 10 m/day, extend to the bottom (300 m), and contribute to deep vertical mixing and the subsequent melting of the ice. These small-scale features are not modeled well with horizontal grids coarser than approximately 2.5 km.

**Citation:** Fujisaki, A., and L.-Y. Oey (2011), Formation of ice bands by winds, *J. Geophys. Res.*, *116*, C10015, doi:10.1029/2010JC006655.

## 1. Introduction

[2] Ice bands are long strips of ice floes often observed near the ice edge; they are generally parallel to but separated from the edge of the main ice pack. The width of an ice band is typically 1–6 km and the band region can be as far as 100 km from the main ice pack [*Wadhams*, 2000; *Ishida and Ohshima*, 2009]. Ice bands are often found during off-ice (wind blowing away from the ice field) or varying wind conditions) [*Johannessen et al.*, 1992; *Wadhams*, 2000; *Ishida and Ohshima*, 2009]. Various generation mechanisms have been suggested to explain how ice bands are formed. *Wadhams* [2000] suggests that fetch-limited wind waves between floes can create bands of high ice concentration under the off-ice wind (wave radiation pressure mechanism). This theory was found to agree with many observations in terms of the width of bands, wind speed, and wind direction [*Wadhams*, 1983; *Johannessen et al.*, 1992; *Wadhams*, 2000; *Ishida and Ohshima*, 2009].

[3] *Muench et al.* [1983], *Sjøberg and Mork* [1985], and *Häkkinen* [1986] suggest that the divergence and convergence of ocean currents due to internal waves can produce ice bands. *Muench et al.* [1983] suggested that ice bands are produced by internal waves under the off-ice wind. Under the hydrostatic approximation, their formulation requires that internal waves be generated under resonance, i.e., the ice edge speed is equal to the baroclinic phase speed. *Sjøberg and Mork* [1985] considered up-ice wind (wind blowing in the opposite direction as the geostrophic velocity shear ($\gg O(0.1\ \text{m s}^{-1})$ over a depth of approximately 10 m) at the ice edge, so that the Ekman transport is away from the ice-edge). They suggested that lee waves can be generated by the moving ice edge when its speed is faster than the first few baroclinic modes. In this study, we call these baroclinic waves simply as lee waves. The idea of lee-wave generation by the moving ice-edge is similar to that of the response of stratified ocean to a moving storm [*Geisler*, 1970]. In both cases, there is a (nearly) discontinuous moving stress field acting on the ocean surface. Across the ice-edge, the stress goes from being large under the ice to small in the ice-free open ocean. In the case of a storm the wind changes from being strong inside the storm to weak outside it. Whereas the movement of a fast-propagating storm is largely independent of the underlying ocean because its propagating speed is usually larger than the first baroclinic phase speed, the movement of ice-edge is intimately coupled to the ocean below. Ice-water interfacial stress generates currents which modify stratification. Stratification changes currents which in turn modify the ice movement. In two hydrographic sections in the East Greenland Sea [*Johannessen et al.*, 1983, Figure 15], small-scale features of 4–8 km are

[1]Graduate School of Frontier Sciences, University of Tokyo, Tokyo, Japan.
[2]Atmospheric and Oceanic Science Program, Princeton University, Princeton, New Jersey, USA.
[3]Now at Cooperative Institute for Limnology and Ecosystems Research, University of Michigan, Ann Arbor, Michigan, USA.


0148-0227/11/2010JC006655

found. The authors suggested that upwelling by winds and mesoscale eddies made the section look complicated and difficult to interpret. They did not discuss the possibility that lee waves may be generated at the ice edge. However, one of their sections was after an up-ice wind event and the wave-like features could be lee waves. *Häkkinen* [1986] applied time-dependent wind in a reduced-gravity model coupled to an ice dynamic model. She found that ice bands were formed when the upper layer was thin and the dynamics was nonlinear. We expect that wind that forces off-ice motion of ice edge is important in producing lee waves, and the time-dependent wind is not essential.

[4] Since lee waves are generated for ice-edge speed greater than the baroclinic phase speed, they are more easily produced by higher modes with lower phase speeds. Previous numerical studies used two-layer or reduced gravity models, and therefore could not be used to assess the effects of higher modes. In this study, we will use two-dimensional (vertical section or *xz*), and three-dimensional ice-ocean coupled models at high resolution to examine the formation of ice bands by lee waves due to higher baroclinic modal responses.

[5] We will also examine how the widths of ice bands are determined in the ice-ocean coupled solution. *Muench et al.* [1983] suggested that the width was determined by internal wavelengths. *Häkkinen* [1986] concluded that the width was approximately twice the Rossby deformation radius. However, these were estimates based on the lowest baroclinic modes, which we shall see do not play a role in the production of lee waves.

[6] The wavelength of lee waves is a function of the difference of the ice-edge speed $u_{edge}$ and the baroclinic phase speed of mode $n$, $c_n$ (details in section 3.2). It seems natural to deduce therefore that the inter-band distance (i.e., width between the crests of ice bands) depends on the wavelength of lee waves. We will show that the inter-band distance is generally larger than the wavelength of lee waves because ice and ocean momentum are coupled by the ice-ocean stress. In other words, ice does not immediately respond to the divergence and convergence of oceanic horizontal velocity. There is some "filtering" effect due to the ice-ocean stress.

[7] Ice-band generation by lee waves depends on small-scale divergences and convergences, which also generate deep vertical motions that penetrate below the Ekman depth. Thus, the formation of ice bands by lee waves can contribute to mixing. The lee-wave solution (see section 3.2) will show that the corresponding scale is shorter than the Rossby deformation radius by a factor that depends on the difference between the ice-edge and baroclinic wave speeds, and is of O(1km) or less, smaller than the typical grid sizes used in general circulation models. By testing different grid sizes, we will evaluate how model resolution can affect the formation of ice bands and accompanying subgrid-scale processes in the marginal ice zones.

[8] Section 2 describes the ice-ocean coupled model and the numerical experiments. Section 3 shows the numerical results and the analytical solution for lee waves due to the moving ice edge. We also explain the low-pass filtering effect due to the ice-ocean stress. The grid-size dependence of ice band formation is studied in section 4. The validity of the two-dimensional (*xz*) solution is examined in section 5, where we compare the two-dimensional solution against the solution from a three-dimensional simulation. In section 6, we summarize our results.

## 2. The Model

### 2.1. Ice-Ocean Coupled Model

[9] A high resolution ice-ocean coupled model is used to resolve the small-scale interactive dynamics between wind, ice and ocean. A vertically sliced two-dimensional domain (*x*-*z*) is used with dimension 250 km × 300 m. The horizontal grid size is 250 m and the vertical layer thickness is 1m in the upper 100 m and linearly increases to 7 m at 300 m depth. In one experiment, we repeated the calculation with a uniform vertical resolution of 1 m and confirmed that the results are virtually identical to those using the linearly coarser grid below 100 m. At the lateral ($x$) boundaries, radiation conditions are used for oceanic velocities, and one-sided advection conditions are used for temperature and salinity. Zero-gradient conditions ($\partial/\partial x = 0$) are used for ice. The ocean model is based on the Princeton Ocean Model, which employs the primitive equations and assumes hydrostatic as well as Bousinnesq approximations [*Mellor et al.*, 2002]. The momentum equation for ice in complex notation (denoted by tildes) is as follows:

$$\frac{\partial \mathbf{u}_i}{\partial t} + jf\mathbf{u}_i = \frac{\tau_{ai}}{\rho_i h_i} + \frac{\tau_{iw}}{\rho_i h_i} - g\nabla\eta + \mathbf{s}_i \tag{1}$$

[10] Here, $j = (-1)^{1/2}$, and the bold symbols denote the complex notation. The ice velocity is $\mathbf{u}_i = u_i + jv_i$. $\rho_i$ and $h_i$ are the ice density and ice thickness, respectively. $\eta$ is the sea surface height. The sea surface tilt force (the third term on the right hand side of equation (1)) and the Coriolis force (the second term on the left hand side of equation (1)) are typically much smaller than the other forcing terms. The ice internal stress is $\mathbf{s}_i$. The ice rheology model uses the elastic-viscous-plastic rheology [*Hunke and Dukowicz*, 1997] and takes account of ice collision [*Sagawa*, 2007]. However, ice motion in this study is mostly in free drift and the ice internal stress is negligible. The $\tau_{ai}$ and $\tau_{iw}$ are wind stress at the air-ice interface and oceanic stress at the ice-water interface, respectively:

$$\tau_{ai} = \rho_a C_{Dai} |\mathbf{u}_a| \mathbf{u}_a \tag{2}$$

$$\tau_{iw} = \rho_w C_{Diw} |\mathbf{u}_w - \mathbf{u}_i| (\mathbf{u}_w - \mathbf{u}_i) \tag{3}$$

[11] Subscripts $a$ and $w$ denote the variables for air and water, respectively. $C_{Dai}$ and $C_{Diw}$ are the air-ice drag and ice-water drag coefficients, respectively. In this study, both skin friction drag and form drag are therefore lumped into the bulk formulae (2) and (3) using $C_{Dai}$ and $C_{Diw}$.

[12] Ice concentration $A$ in each cell is calculated using a semi-Lagrangian advection scheme [*Rheem et al.*, 1997; *Sagawa and Yamaguchi*, 2006]. The sea surface stress $\tau_w$ is then calculated using a combination of the ice-water stress $\tau_{iw}$ and the air-water stress $\tau_{aw}$ weighted by $A$.

$$\tau_w = \tau_{iw} A - \tau_{aw}(1 - A) \tag{4}$$

**Table 1.** Model Parameters

| Name | Description | Value |
|---|---|---|
| $dt_{ext}$ | time step in external mode | 1.5 sec |
| $dt_{int}$ | time step in internal mode and ice thermodynamic model | 45 sec |
| $C_{Dai}$ | air-ice drag coefficient | $3.0 \times 10^{-3}$ |
| $C_{Daw}$ | air-water drag coefficient | $1.5 \times 10^{-3}$ |
| $C_{Diw}$ | ice-ocean drag coefficient | $9.0 \times 10^{-3}$ |
| $c_h$ | ice-ocean heat transfer coefficient | $5.0 \times 10^{-3}$ |
| $\rho_a$ | density of the air | 1.247 kg m$^{-3}$ |
| $\rho_i$ | density of sea ice | 910.0 kg m$^{-3}$ |
| $L_i$ | melting latent heat of sea ice | $3.3 \times 10^5$ J kg$^{-1}$ |

where

$$\tau_{aw} = \rho_a C_{Daw} |\mathbf{u}_a| \mathbf{u}_a \tag{5}$$

and $C_{Daw}$ is the air-water drag coefficient. Generally, this is smaller than the air-ice drag coefficient $C_{Dai}$ because ice surface is rougher than that of open water due to ridged and rafted floes as well as sidewalls of individual floes (i.e., freeboard). Wind stress is therefore larger over ice than over open water. In a quasi-steady state and in the free drift regime, $\tau_{iw}$ is primarily balanced by $\tau_{ai}$. Therefore $\tau_w$ is larger over ice-covered water, which creates Ekman convergence (or divergence) necessary for lee-wave generation discussed in section 3.

[13] Equation (4) shows that the wind stress over ice is not simply equal to the stress to the sea surface because of the ice-water stress $\tau_{iw}$ (equation (3)). In other words, the wind stress is not instantaneously transmitted through the ice to the sea surface – there is a finite momentum transfer rate which, as we will show in section 3.3, causes a smoothing effect on ice-band formation.

[14] Although equation (4) is a realistic treatment of the sea surface stress, it cannot be easily used in analytical solution. Therefore, in addition to equation (4), we also tested a simpler stress formula:

$$\tau_w = \begin{cases} \tau_{ai} & A > 0 \\ \\ \tau_{aw} & A = 0 \end{cases} \tag{6}$$

which implies an instantaneous transfer of momentum from wind over ice to the sea surface. This simpler formulation allows for an analytical solution that can be compared with the corresponding numerical solution. The formula represents the stress as a step function moving at the speed of the ice edge.

[15] In this study, sea-surface heat flux is only through the ice-ocean interface, given by:

$$H_{iw} = \rho_w c_p c_h u^* \left(T_m - T_{mf}\right) \tag{7}$$

where $T_m$ is the mixed-layer temperature and $T_{mf}$ is the freezing temperature in the mixed layer. $T_m$ is set equal to the temperature at the first grid point near the surface, and $T_{mf}$ is calculated as a function of the salinity at first grid point near the surface [*Millero*, 1978]. The specific heat of seawater $c_p$ is set to 4000 J/kg/K. The friction velocity is $u^* = \sqrt{|\tau_w|/\rho_w}$ and $c_h = 0.005$ is the ice-ocean heat transfer coefficient [*McPhee et al.*, 2008]. In the model, $H_{iw}$ (>0) causes ice to melt, which leads to ice thinning $\Delta h_i = -H_{iw}/L_i$, where $L_i$ is the latent heat of fusion per unit volume of ice, and which also increases the stratification beneath the ice due to efflux of freshwater. In order to focus on the ice-ocean interaction, we exclude heat and buoyancy fluxes at the open water surface. We will see that strong vertical motions by lee-waves result in upward heat flux ($H_{iw} > 0$), ice-melting, and non-negligible change in the ice thickness near the ice edge. Ice thickness can also change by wind-forced ice convergence (and divergence), but this is negligible in this study since the applied wind field is uniform and the model ice is mostly in free drift.

[16] The model parameters are given in Table 1.

[17] Initially, ice is at rest with uniform ice concentration $A = 0.8$ on the left side ($0 \leqq x \leqq 60$ km) of the $x$-$z$ domain (250 km × 300 m), and is in quasi-equilibrium through ice-ocean heat transfer with the underlying ocean. These initial conditions were obtained by placing an ice sheet of uniform thickness at $x$ = 0–60 km atop a resting ocean with uniform potential temperature (= 3°C) and salinity (= 35 psu) through a long-term (120 days) integration without any forcing except the (slow, diffusive) ice-ocean heat transfer. A quasi-steady state is reached at the end of this spin-up, whereby the coupled ice-ocean field is very slowly evolving at time scales (>O(100) days) much longer than the time scales of ice-band formation after the wind is applied. The end of this spin-up is then taken as the initial state for all subsequent experiments when wind is applied. The corresponding ice thickness is 2 m, which is thicker than what is typically observed ($\gg$1 m) in a marginal ice zone, but it is not too unrealistic. Since thick ice moves slower than thin ice, this choice allows us to use a smaller domain.). We have repeated the standard experiment (Expt. 0; see below) with an initial ice thickness = 1 m. The two results are similar since the faster, thinner ice also generates lee waves.

[18] At the initial state (i.e., end of 120-day spin-up), cold and fresh layer is below the model ice and the along-ice water velocity, which is weak with speeds ≈0.05 m s$^{-1}$, is in geostrophic balance with the density field. Wind with speed = 5 m s$^{-1}$ is then applied in the positive $y$-direction (an up-ice wind). The wind is slowly ramped to 5 m/s in 5 days using a sinusoidal function:

$$v_a = \begin{cases} 5 \sin(\pi t/10) \quad \text{ms}^{-1} & 0 \leq t \leq 5\text{d} \\ \\ 5 \quad \text{ms}^{-1} & 5\text{d} \leq t \end{cases}$$

[19] Up-ice wind is favorable for sea-ice divergence off the ice-edge in the northern hemisphere, but water under the ice downwells at the ice edge by Ekman convergence. Note that apart from the ramping, the wind is time-independent.

### 2.2. Numerical Experiments

[20] The numerical experiments are listed in Table 2. Experiment 0 is the standard experiment, where an up-ice wind is applied and the sea surface stress is calculated using equation (4). Experiment 1 uses the step-function stress formula (equation (6)) to compare with the analytical solution. The ice-water stress $\tau_{iw}$ used in the momentum equation for ice equation (1) is still a function of the relative velocity of ice and ocean equation (3), so that ice bands

**Table 2.** Numerical Experiments

| Experiment | Description |
|---|---|
| Expt. 0 | Standard experiment. |
| Expt. 1 | Step-function experiment. Sea surface stress is given by equation (6). |
| Expt. 2 | Strong-wind experiment. Wind speed $v_a$ = 10 m s$^{-1}$. |
| Expt. 3 | No-LPF (no-low-pass-filter) experiment. Sea ice advects by the sea surface velocity. Sea surface stress is given by equation (6) |
| Expt. 4 | Down-ice wind experiment. Wind speed $v_a$ = −5 m s$^{-1}$. |
| Expt. 5 | Off-ice wind experiment. Wind speed $u_a$ = 5 m s$^{-1}$. |
| Expt. 6 | Initial ice concentration with 4 km wedges. |
| Expt. 7 | Coarser-resolution experiments. $\Delta x$ = 1 km, 2.5 km, and 5 km. |
| Expt. 8 | Three-dimensional experiment with $\Delta x = \Delta y$ = 1 km; $\Delta z$ = 1 m in the upper 10 m; periodic in $y$. |

can still be generated by convergence and divergence. Experiment 2 is the same as Expt. 0, except that the wind is two-times stronger ($v_a$ = 10 m s$^{-1}$). Experiment 3 is a "no-low-pass-filter (No-LPF)" case in which sea ice is advected by the sea surface velocity only, and therefore $\tilde{u}_i = \tilde{u}_w$. In this experiment, the step function stress equation (6) is applied to the sea surface. The motivation for this experiment will be discussed in section 3.3. In Expts. Four and 5, down-ice and off-ice winds respectively are tested. Initial ice concentration with narrow openings within the ice cover (hereinafter referred to as "wedges") of 4 km is tested in experiment 6 to examine the nature of the resulting lee waves compared to those produced by a single ice edge. Experiments with coarser resolutions of 1 km, 2.5 km and 5 km are conducted in experiment 7 to examine how well lee waves can still be resolved and to check the sensitivity of the solution, e.g., vertical velocity and melt rate, to the different resolutions. We will show that 1 km-resolution is approximately the limit with which ice-bands generated by lee waves can still be resolved.

[21] The experiments above are limited to a two-dimensional ($xz$) domain. It is necessary to show the validity of the two-dimensional solutions and to confirm that ice bands are also formed, at least within the period (O(10 days)) of the two-dimensional experiments, by wind-induced lee waves in a more realistic three-dimensional setting. We

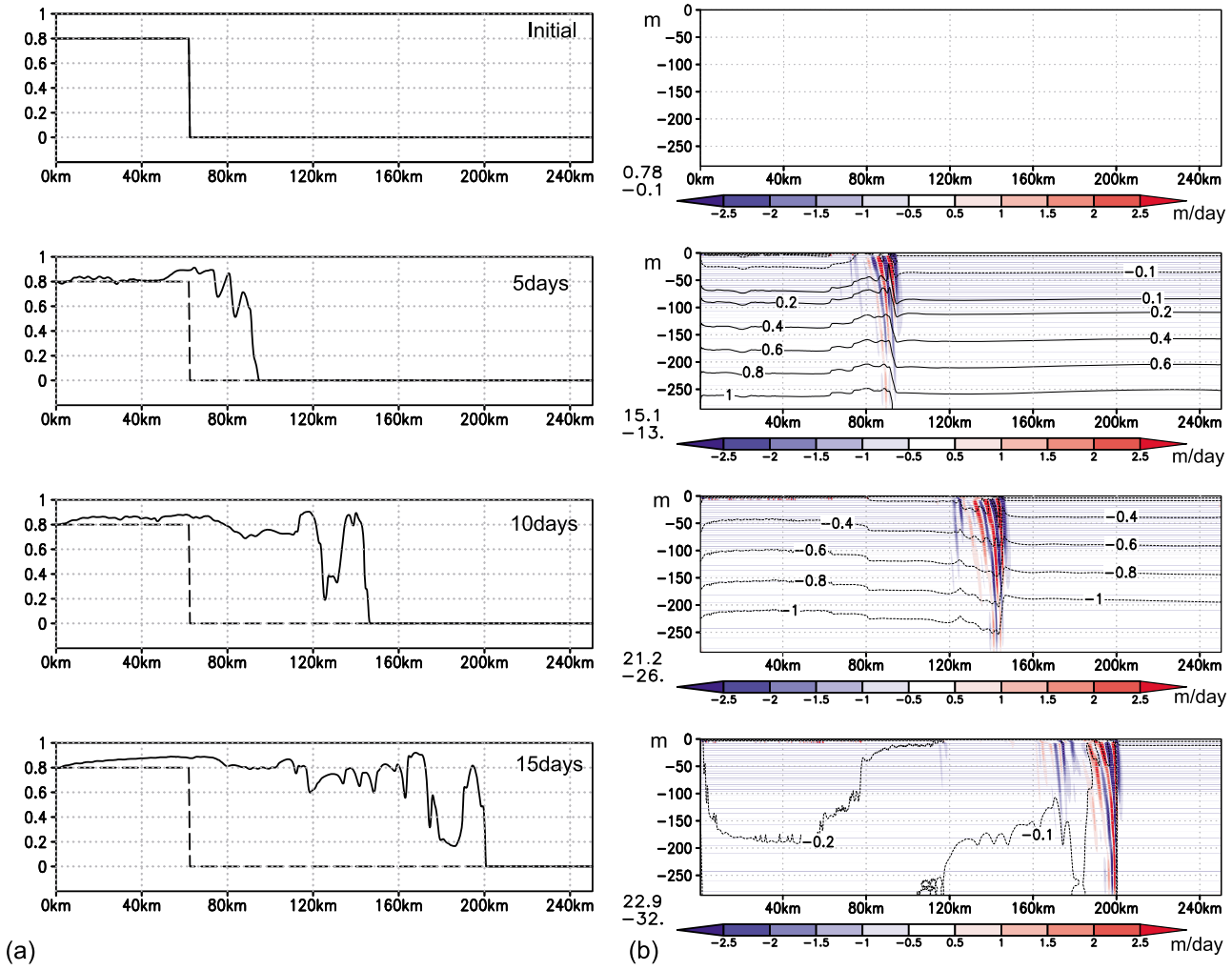


**Figure 1.** Temporal evolution of (a) ice concentration $A$ (the dashed line is the initial ice concentration) and ice thickness (normalized by initial thickness of 2 m; blue), and (b) vertical velocity $w$ (m/day) (shades), and stream function $\phi$ (Sv) (contours). Maximum and minimum values for $w$ (m/day) are shown at the lower left corner.

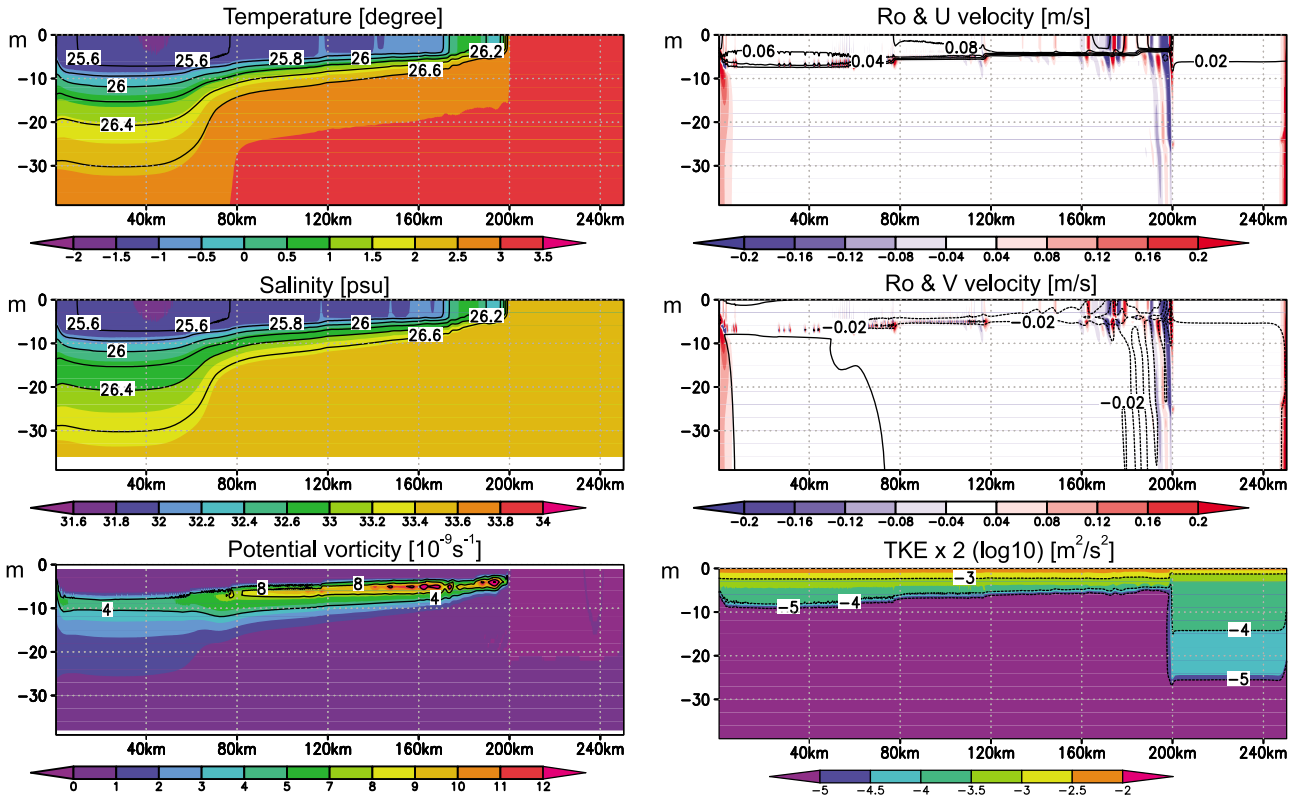


**Figure 2.** Temperature $T$ and salinity $S$ (shadings) with contours of potential density $\sigma_\theta$ superimposed, horizontal velocity $u_w$ and $v_w$ (shadings) with contours of Rossby numbers $Ro = \partial v/\partial x \cdot f^{-1}$, potential vorticity $PV$, and twice the turbulent kinetic energy after 15 days of simulation for Expt. 0.

therefore conduct, in the final experiment (Expt. 8), a three-dimensional simulation with a uniform horizontal resolution of 1 km in a square channel of 250 km × 250 km and constant depth = 300 m. A vertical grid size of 1m is kept (as in the two-dimensional experiments) in the upper 10m to resolve the thin surface layer below sea ice. Below that, from $z = -10$ m to $z = -100$ m, the grid size is 2 m, and it then linearly increases to 16 m at the bottom. Periodic conditions are used in the $y$-direction. All other model parameters, initial conditions and forcing are otherwise identical to Expt. 0.

## 3. Numerical Results and Analytical Solution

### 3.1. Numerical Results

[22] Under the up-ice wind, ice concentration $A$ develops uneven "bumpy" distribution after 5 days (Figure 1a). We define an ice band as one waveshape between two ice concentration minima. The width for the first band after 10 days is about 20 km. Wave-like vertical velocity field associated with ocean's convergence and divergence can be seen below the band (Figure 1b), and they are lee waves. The wavelength is about 6 km, and the amplitude for the vertical velocity is the order of 10 m/day. The stress acting on the water under the ice is generally much larger than that over the open water due in part to the different drag coefficients even though the relevant velocities are much smaller. The wind stress is therefore effectively a step function moving at the ice-edge velocity $u_{edge}$. This moving stress can generate lee waves [*Geisler*, 1970; *Gill*, 1982] when $u_{edge}$ exceeds the baroclinic phase velocity $c_n$, i.e., supercritical condition $u_{edge} > c_n$. The wave-like vertical motions in Figure 1b are lee waves generated by the moving ice-edge and ice bands are created because the ice is dragged by the convergence and divergence of oceanic velocity. The vertical downwelling and upwelling perturbation cells (Figure 1b) produce an upward heat flux, resulting in significant melting near the ice edge. By day15, 40% of the initial ice (thickness) has melted within a 30 km distance behind the ice edge (Figure 1a). Also, cold and fresh water is advected (by Ekman current) with the ice edge over fluid that is warmer but saltier. This process creates a thin stratified layer just below the mixed layer beneath the ice. In terms of potential vorticity, $PV = -\vec{\omega}_{\mathbf{a}} \cdot \nabla\rho/\rho_0$ where $\vec{\omega}_{\mathbf{a}}$ is the absolute vorticity vector, the buoyancy gradient is directed on-ice ($\partial b/\partial x < 0$, $b = -g\Delta\rho/\rho_0$), and that combines with the up-ice stress ($\tau_w^y > 0$) to produce a downward $PV$ flux across the ice-water interface that increases the $PV$ just beneath the ice [*Thomas*, 2005] that is clearly seen in Figure 2. The largest $PV$ is immediately under the ice-edge because of both local downward flux and advection from upstream (i.e., farther behind the ice-edge). The $u_w$ plot shows convergence and divergence regions that account for the unevenness of $A$ seen in Figure 1 at $t = 15$ days. Because of the strong stratification, turbulence is much strongly damped under the ice than over the ocean water ahead of the ice-edge (see the TKE plot of Figure 2). The resulting reduced friction allows ice edge to move faster, i.e., $u_{edge}$ becomes stronger (than otherwise without the strong stratification). Moreover, the weak stratification ahead of the ice-edge tends to reduce $c_n$

and in combination with the strong $u_{edge}$ favors the establishment of supercritical conditions and the generation of lee waves. These inferences are supported by results from other experiments below, as well as by the analytical solution in section 3.2 where we will also explain why the inter-band distances are larger than the lee-wavelengths (Figure 1).

[23] Figure 3 compares the ice and oceanic variables 15 days after the up-ice wind is applied for the standard experiment (Expt. 0), the step-function stress experiment (Expt. 1), and the strong-wind experiment (Expt. 2). In Expt. 0, since the surface stress continuously changes depending on the ice concentration $A$ (see equation (4)), the lead ice band can generate secondary (and weaker) lee waves due to the large change in $A$ (hence also a large change in the corresponding stress) behind. This produces trailing small-scale features in "$A$" further behind (Figure 1b and Figure 3b, left). For Expt. 1, the surface stress is an "on-off" function of $A$ given by equation (6). Therefore, only main lee waves exist.

[24] In both cases, lee waves are dampened far behind the ice edge because the flow there is subcritical ($u_{edge}/c_n < 1$) due to the existence of larger baroclinic phase velocity $c_n$ caused by the strong stratification under the ice (Figure 2). Just behind the lead ice band, lee waves in Expt. 0 ($x \sim 190$ km, Figure 3a) are more strongly dampened compared to those in Expt. 1 ($x \sim 220$ km, Figure 3b). The reason is because in Expt. 0, the sea surface stress $\tau_w$ depends in part on $\tau_{iw}$, which in turn depends on the relative velocity between ice and ocean (see equations (4) and (3)), whereas in Expt.1, $\tau_w$ depends entirely on the wind. The $\tau_{iw}$ dampens lee waves (in Expt. 0) due to the negative feedback by the water velocity $\mathbf{u}_w$.

[25] In the strong-wind experiment (Expt. 2, Figure 3, right), more intense lee waves are seen because of the larger $\Delta_u = |\mathbf{u}_w - \mathbf{u}_i|$. On the other hand, the ice-bands are less clearly defined, as the corresponding spatial scales are shorter than Expt. 0 with weaker wind. This is an interesting (counter-intuitive) result that will be discussed in section 3.3. We will show that smoothing by the ice-ocean stress is weakened by larger $\Delta u$.

### 3.2. An Analytical Treatment of Lee-Wave Generation and Numerical Results

[26] In this subsection, we derive an analytical solution for lee-wave generation and compare the solution with the numerical model solution. Linear shallow water equations for the continuously stratified fluid are used to study the ocean response to a moving ice edge.

$$\frac{\partial u_w}{\partial t} - f v_w = -\frac{1}{\rho_0}\frac{\partial p'}{\partial x} + \frac{1}{\rho_0}\frac{\partial X}{\partial z} \tag{8}$$

$$\frac{\partial v_w}{\partial t} + f u_w = -\frac{1}{\rho_0}\frac{\partial p'}{\partial y} + \frac{1}{\rho_0}\frac{\partial Y}{\partial z} \tag{9}$$

$$\frac{\partial \eta}{\partial t} = -H\left(\frac{\partial u_w}{\partial x} + \frac{\partial v_w}{\partial y}\right) \tag{10}$$

[27] Here, $p'$ is a perturbation of pressure, and $X$ and $Y$ are stresses in $x$ and $y$ directions, respectively. At $z = 0$, $X$ and $Y$ are the wind stress and ice-water stress weighted by ice concentration (see equation (4)). We assume that the stress is a step function moving at the ice edge's speed $u_{edge}$. For a $y$-component stress, the ocean feels larger stress $Y_s + \Delta Y_s$ under ice covered region ($x \leqq u_{edge}t$).

$$Y = \begin{cases} Y_s + \Delta Y_s & x \le u_{edge}t \\ Y_s & x > u_{edge}t \end{cases} \tag{11}$$

and a similar expression applies for the $x$-component stress $X_s + \Delta X_s$. Each of the variables $u_w$, $v_w$, $p'$ and the stress terms are expanded in normal modes [*Gill*, 1982]:

$$p' = \sum_{n=0}^{\infty} \tilde{\eta}_n(x,y,t)\hat{p}_n(z) \tag{12}$$

$$(u_w, v_w) = \sum_{n=0}^{\infty} (\tilde{u}_n(x,y,t), \quad \tilde{v}_n(x,y,t))\hat{p}_n(z)/\rho_w g \tag{13}$$

$$\rho_w^{-1}(\partial X/\partial z, \partial Y/\partial z) = \sum_{n=0}^{\infty} \left(\tilde{X}_n(x,y,t), \tilde{Y}_n(x,y,t)\right)\hat{p}_n(z)/\rho_w g \tag{14}$$

where a hat and a tilde denote the vertical and horizontal structures, respectively.

[28] Substitute equations (12)–(14) into equations (8)–(10), and assume that the $y$-derivatives are zero,

$$\frac{\partial \tilde{u}_n}{\partial t} - f\tilde{v}_n = -g\frac{\partial \tilde{\eta}_n}{\partial x} + \tilde{X}_n \tag{15}$$

$$\frac{\partial \tilde{v}_n}{\partial t} + f\tilde{u}_n = \tilde{Y}_n \tag{16}$$

$$\frac{\partial \tilde{\eta}_n}{\partial t} = -H_n\frac{\partial \tilde{u}_n}{\partial x} \tag{17}$$

$H_n$ denotes the equivalent depth for the $n$th mode. These equations can be manipulated into an equation for $\tilde{\eta}_n$.

$$\frac{\partial^2 \tilde{\eta}_n}{\partial x^2} - \frac{1}{gH_n}\left(\frac{\partial^2}{\partial t^2} + f^2\right)\tilde{\eta}_n = \frac{1}{g}\frac{\partial \tilde{X}_n}{\partial x} + \frac{f}{g}\int \frac{\partial \tilde{Y}_n}{\partial x}dt \tag{18}$$

[29] It is useful to write this equation in non-dimensional form with subscripts $k$'s denoting dimensionless variable:

$$\left(1 - U_{kn}^2\right)\frac{\partial^2 \eta_{kn}}{\partial \zeta_k^2} - \eta_{kn} = \frac{\Delta\tau H_n f c_n}{\rho_w}\left[\frac{\partial X_{kn}}{\partial \zeta_k} + \int \frac{\partial Y_{kn}}{\partial \zeta_k}dt_k\right] \tag{19}$$

where

$$U_{kn} = u_{edge}/c_n, \quad \eta_{kn} = \eta/H_n, \quad \zeta_k = \zeta/R_n, \quad X_k = X/\Delta\tau,$$

$$X_k = X/\Delta\tau, \quad t_k = ft, \quad \zeta = x - u_{edge}t, \text{ and } R_n = c_n/f$$

is the Rossby deformation radius for the $n$th mode. Note that since ice velocity $u_{edge}$ in general differs from the ocean's surface velocity, $U_{kn}$ is not the same as the internal Froude number. Nonetheless, we will refer to $U_{kn} < 1$ as subcritical condition because equation (19) is then elliptic, and $U_{kn} > 1$ as supercritical condition since equation (19) then becomes hyperbolic (see below). The right hand side is evaluated using the step function given in equation (11) (*Gill* [1982]; for simplicity we set $\Delta X_s = \Delta Y_s = \Delta\tau$).

$$\left(1 - U_{kn}^2\right)\frac{\partial^2 \eta_{kn}}{\partial \zeta_k^2} - \eta_{kn} = \frac{\Delta\tau H_n f c_n}{\rho_w}[-\delta(\zeta_k) + H_o(-\zeta_k)/U_{kn}] \tag{20}$$

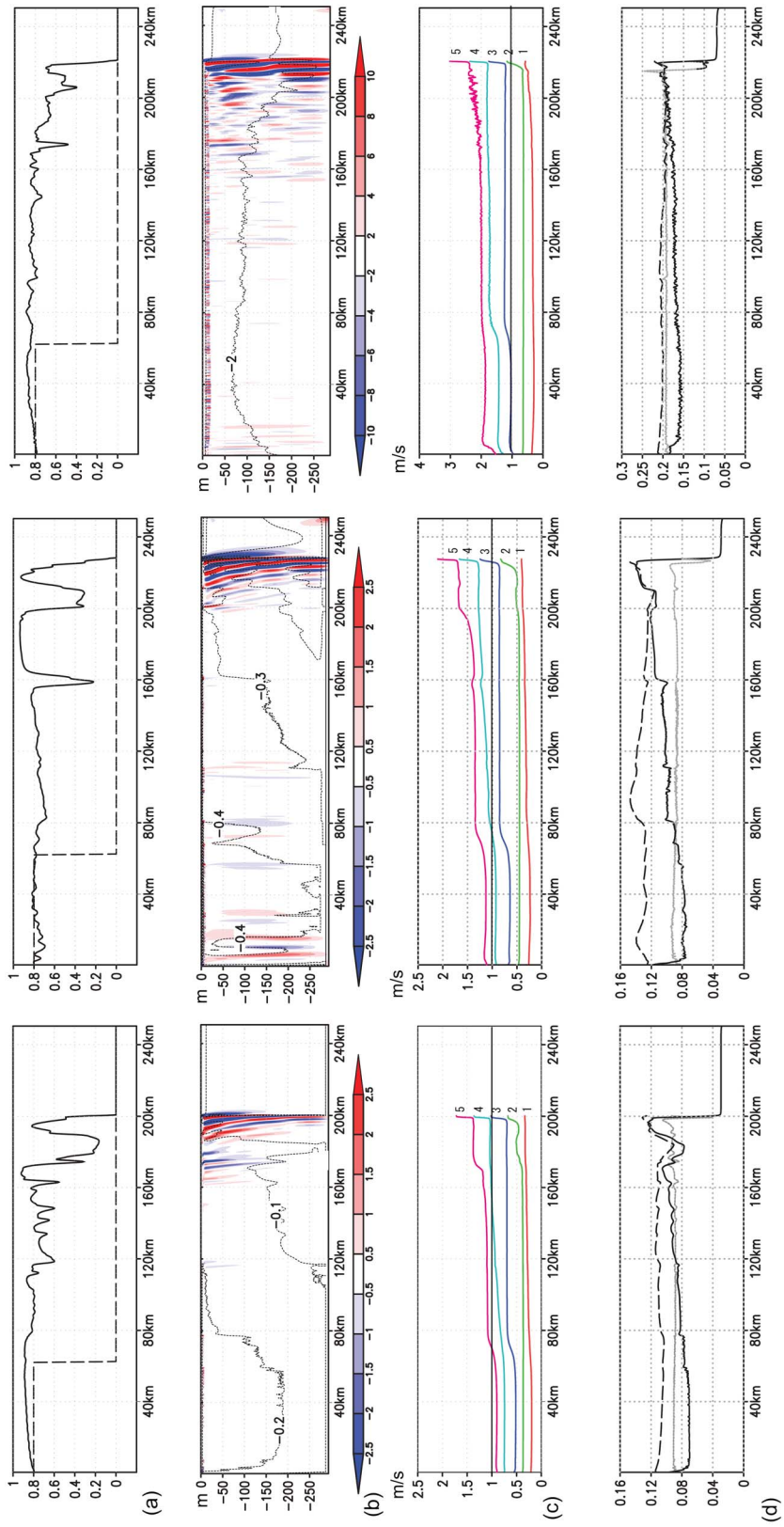


**Figure 3.** Simulation results at day#15: (left) Standard experiment (Expt. 0) where sea surface stress is a function of variable ice concentration $A$. (middle) Step-function experiment (Expt. 1) where sea surface stress is determined only by ice's presence. (right) Strong-wind experiment with $\nu_a = 10$ m s$^{-1}$ (Expt. 2). The variables are, from top to bottom: (a) ice concentration $A$, (b) vertical velocity $w$ (m/day) (shades) and stream function $\phi$ [Sv] (contours), (c) ratio of the ice-edge velocity to the baroclinic phase velocity $u_i/c_n$, (mode number and the line of $u_i/c_n = 1$ are shown), (d) sea surface velocity $u_w$ (solid line), ice velocity $u_i$ (dashed line), and the magnitude of the relative velocity $\Delta u = |\mathbf{u}_w - \mathbf{u}_i|$ (gray dotted line); units are in m s$^{-1}$.

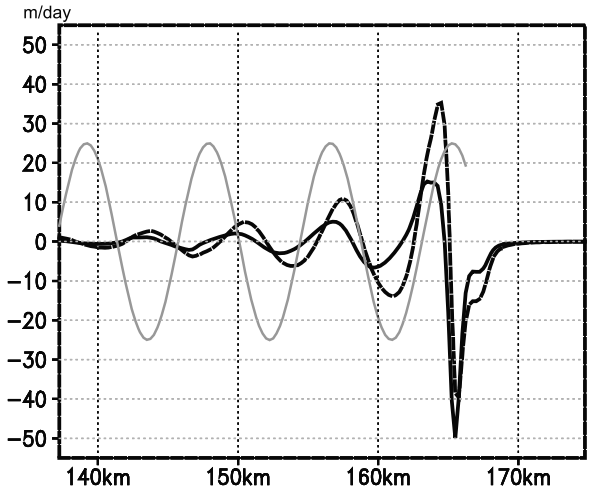


**Figure 4.** Vertical velocities $w$ (m/day). Black lines are from the step-function experiment (Expt. 1): solid line is at 10 m depth, and dashed line is at 20 m depth. Grey line is derived from equation (31) with a wavelength 8.7 km and amplitude 25 km.

[30] For subcritical condition $U_n < 1$, equation (20) is elliptic with decaying solution (no lee waves). For supercritical condition $U_n > 1$, equation (20) is hyperbolic and solution contains lee waves.

[31] The $\tilde{X}_n$, $\tilde{Y}_n$ can be expressed using the equivalent forcing depth $H_n^F$ [*Gill*, 1982] as:

$$\left(\tilde{X}_n, \tilde{Y}_n\right) = (X_s, Y_s)/\rho_w H_n^F \tag{21}$$

$$H_n^F = \frac{\rho_w g}{H_{mix}} \frac{\int_{-H_{mix}}^{0} \hat{p}_n dz}{\int_{-H}^{0} \hat{p}_n^2 dz} \tag{22}$$

[32] We now specialize equation (20) to the case of an up-ice wind only ($X_s = 0$, and $Y_s$ given by equation (11)), which then becomes, after reverting to dimensional form:

$$-\left(\frac{u_{edge}^2 - c_n^2}{f^2}\right)\frac{\partial^2 \tilde{\eta}_n}{\partial \zeta^2} - \tilde{\eta}_n = \frac{c_n^2 \tilde{Y}_n}{f g u_{edge}} = \begin{cases} a_n(Y_s + \Delta Y_s) & \zeta \le 0 \\ a_n Y_s & \zeta > 0 \end{cases} \tag{23}$$

$$a_n = \frac{c_n^2}{f \rho_w g H_n^F u_{edge}} \tag{24}$$

where $\zeta = R_n \xi$.

[33] For a slowly moving ice edge ($u_{edge} < c_n$), equation (23) is elliptic. With a continuity condition at $\zeta = 0$ and non-divergence at $\zeta = \infty$, the solution is decaying behind the ice edge:

$$\tilde{\eta}_n = \begin{cases} \frac{a_n \Delta Y}{2}(\exp(\alpha\zeta) - 2) + a_n Y & \zeta \le 0 \\ a_n Y & \zeta > 0 \end{cases} \tag{25}$$

$$\alpha^2 = \frac{f^2}{c_n^2 - u_{edge}^2} \tag{26}$$

[34] For a fast-moving ice edge ($u_{edge} > c_n$), equation (23) is hyperbolic. With the additional continuity conditions $\partial\tilde{\eta}_n/\partial\zeta$ at $\zeta = 0$ and no-wave condition ahead the ice edge, a lee-wave solution results:

$$\tilde{\eta}_n = \begin{cases} a_n \Delta Y(\exp(j\kappa\zeta) - 1) + a_n Y & \zeta \le 0 \\ a_n Y & \zeta > 0 \end{cases} \tag{27}$$

$$\kappa^2 = \frac{f^2}{u_{edge}^2 - c_n^2} \tag{28}$$

[35] In the numerical results, supercritical condition, i.e., $u_{edge} > c_n$ occurs at the ice edge for mode 3 in Expts.0 and 1, and for mode 2 in Expt. Two (Figure 3). In Expts. 0 and 1, the flow becomes subcritical ($u_{edge} < c_n$) behind the ice edge so that waves decay far behind the ice edge in these experiments. On the other hand, the vertical velocity in Expt. Two still shows wave motion behind the ice edge because the mode 3 remains supercritical (Figure 3). The fact that modes 4 and 5 are supercritical behind the ice edge but no wave is seen implies that contributions from modes higher than 3 are small.

[36] We can estimate the vertical velocity based on the normal-mode solution equations (21), (26) and (27) by solving for $\hat{p}_n(z)$ from:

$$\frac{d^2 \hat{p}_n}{dz^2} + \frac{N^2}{c_n^2}\hat{p}_n = 0 \tag{29}$$

where the buoyancy frequency $N^2$ is obtained from the numerical model, and $\hat{p}_n(z)$ is normalized such that $\hat{p}_n(0) = \rho_w g$. From equations (8) and (9) we obtain:

$$\left(\frac{\partial^2}{\partial t^2} + f^2\right)\frac{\partial u_w}{\partial x} = -g\frac{\partial}{\partial t}\left(\frac{\partial^2 \eta}{\partial x^2}\right) \tag{30}$$

[37] Assuming the same phase velocity for $u_w$ as for $\eta$, $\partial u_w/\partial x$ can be derived by equation (30). The continuity equation $\partial u_w/\partial x + \partial w_w/\partial z = 0$ and taking the real part then give:

$$w(z) = \int_z^0 -\frac{\partial u_w}{\partial x} dz = \int_z^0 -\frac{g a_3 \Delta Y \kappa^3 u_{edge}}{\left(\kappa u_{edge}\right)^2 - f^2}\sin(\kappa\zeta) dz \tag{31}$$

$$|w(-H_{mix})| = \frac{g a_3 \Delta Y \kappa^3 u_{edge} H_{mix}}{\left(\kappa u_{edge}\right)^2 - f^2} \tag{32}$$

[38] Note that we have specified the third mode to compare with the numerical results. The mixed layer depth $H_{mix}$ is estimated as 8m (see temperature and density in Figure 2), and therefore $w \gg 25$ m/day. This analytical value agrees well with the numerical model result near the ice edge (Figure 4). Behind the ice edge, numerical model's lee waves decay because of the subcritical condition. The numerical model-predicted wavelength $\lambda = 2\pi/\kappa$ for lee waves are $\gg$6 km (Expt. 1, in Figure 4), which is a little shorter than, but not inconsistent with the 8.7 km estimated from equation (28).

[39] In case of a down-ice-wind case (Expt. 4), warmer but saltier open-ocean water is advected toward and under the ice. The *PV*-flux is upward (a loss) and the fluid below the

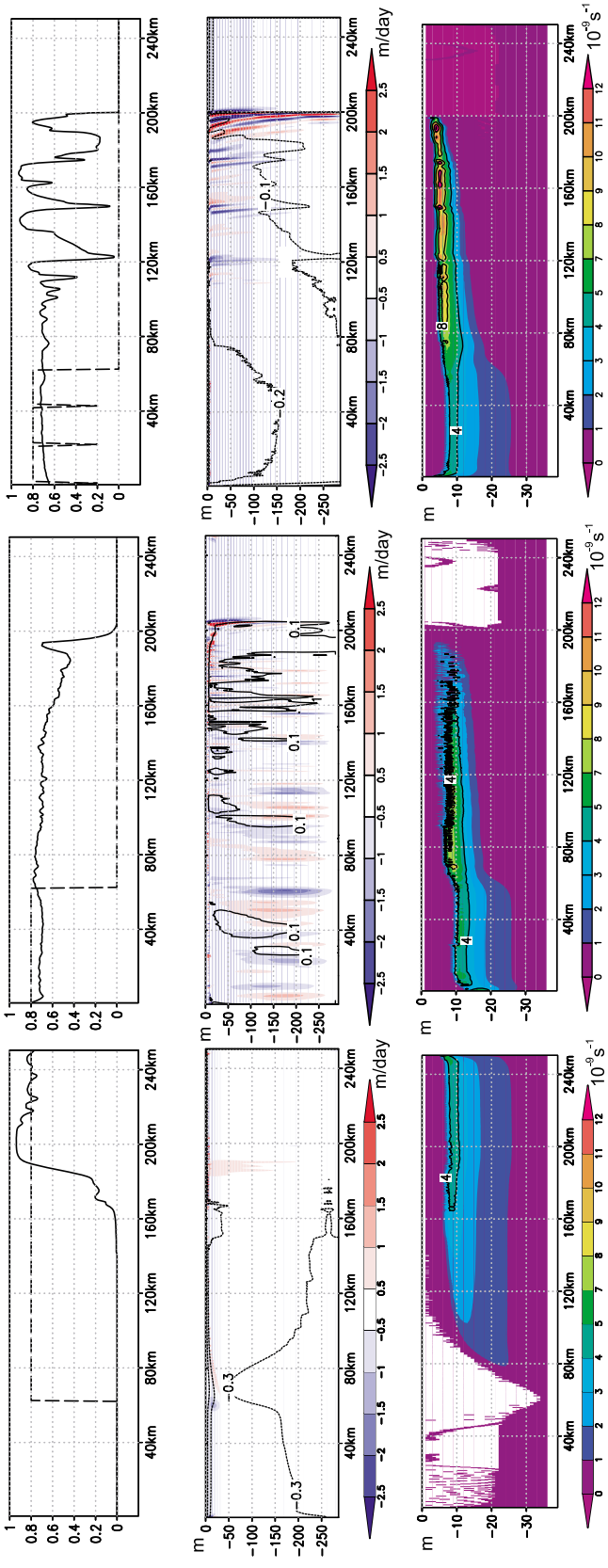


**Figure 5.** Experiment results at day#15 for (a) down-ice-wind experiment (Expt. 4), (b) off-ice-wind experiment (Expt. 5), and (c) initial ice concentration with 4 km-wide wedges (Expt. 6). (top) Ice concentration $A$, (middle) vertical velocity $w$ (m/day) with stream function $\phi$ (Sv), and (bottom) potential vorticity $PV$ ($10^{-9}$ s$^{-1}$) are shown.

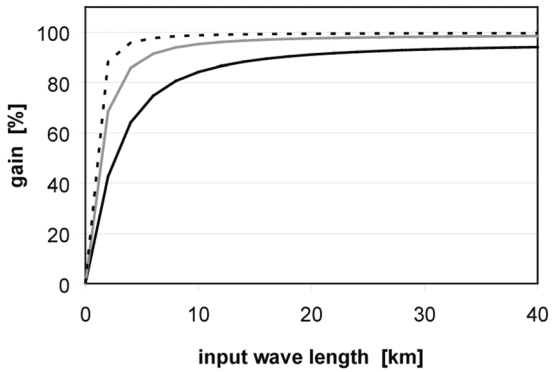


**Figure 6.** Gain $G = |\mathbf{u}_i/\mathbf{u}_w|$ plotted as a function of wavelength of $u_w$. Solid: $\alpha = 2.5 \times 10^{-4}$ s$^{-1}$ ($\Delta u = 0.05$ m s$^{-1}$). Thin: $\alpha = 5.1 \times 10^{-4}$ s$^{-1}$ ($\Delta u = 0.1$ m s$^{-1}$). Dashed: $\alpha = 1.0 \times 10^{-3}$ s$^{-1}$ ($\Delta u = 0.2$ m s$^{-1}$).

ice tends toward a well-mixed state because of unstable convection (both upright and slantwise convection). Figure 5 (left) shows that the potential vorticity is low under the ice, and neither lee waves nor ice bands are generated.

[40] The off-ice wind Expt. Five (Figure 5, middle) does not produce clear lee waves and ice bands even though the wind drives ice edge offshore similar to the case under the up-ice wind experiment (see Figure 1). Instead, there is just a strong dipole of upwelling and downwelling at the ice edge in Expt. 5, which could be due to the oceanic convergence beneath the ice edge, rather than wave generation. Under the off-ice wind, the forcing function (the right hand side of equation (18)) is a delta function, and this makes it difficult to find a wave solution that satisfies the continuity condition at $\zeta = 0$ even when the condition is supercritical. It is known that the off-ice wind generates ice bands by the wave pressure radiation [*Johannessen et al.*, 1992; *Wadhams*, 2000; *Ishida and Ohshima*, 2009], which is not taken into account in this study. It appears the off-ice wind is not particularly efficient in producing ice bands by the lee-wave generation mechanism.

[41] Experiment 6 (Figure 5) has an initial ice concentration consisting of narrow wedges of 4 km, so there are gaps of sea surface stress. After 15 days, the *PV* field is similar to Expt. 0 (Figure 2), but higher-mode lee waves are generated behind wedges. Such ice wedges are typical in the marginal ice zones: For example, fetches created by the wave pressure radiation [*Wadhams*, 1983, 2000] may produce wedges, and the resulting lee waves forced by wind may significantly contribute to mixing.

### 3.3. Smoothing Effects by Ice-Ocean Stress

[42] As noted previously, the dominant wavelength of the vertical velocity $w$ is shorter than the inter-band distance (e.g., Figure 1). We now show that this is because of the smoothing effect of the ice-ocean stress equation (3). Since the momentum is transferred at a finite rate, the high-frequency component is lost in the transfer. To see this, consider the linear response of ice to ocean in the

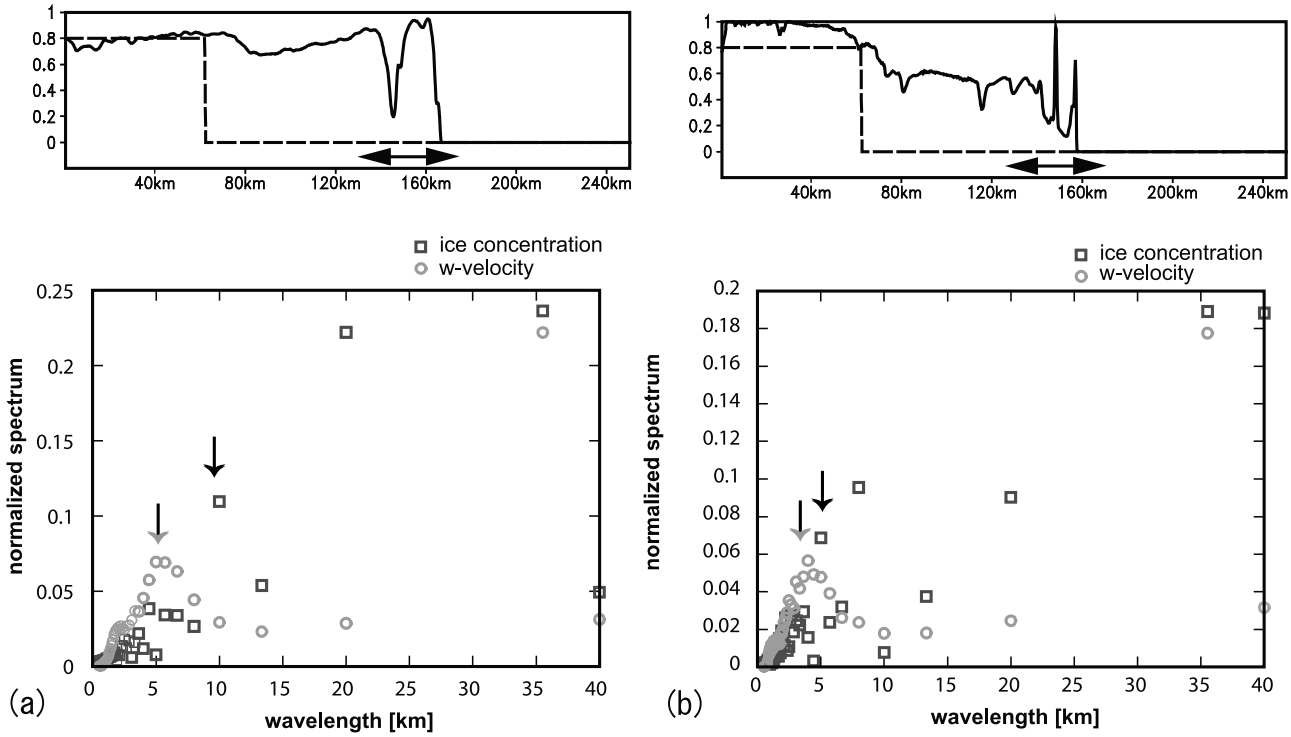


**Figure 7.** (top) Ice concentration at day10 for ice concentration $A$ and (bottom) spectrum of vertical velocity $w$. (a) Step-function-stress experiment (Expt. 1), (b) No-LPF experiment (Expt. 3). Regions where the spectra are calculated are shown in Figure 7, top. In Figure 7b, local peaks for vertical velocity and ice concentration are shown by gray and black arrows respectively.

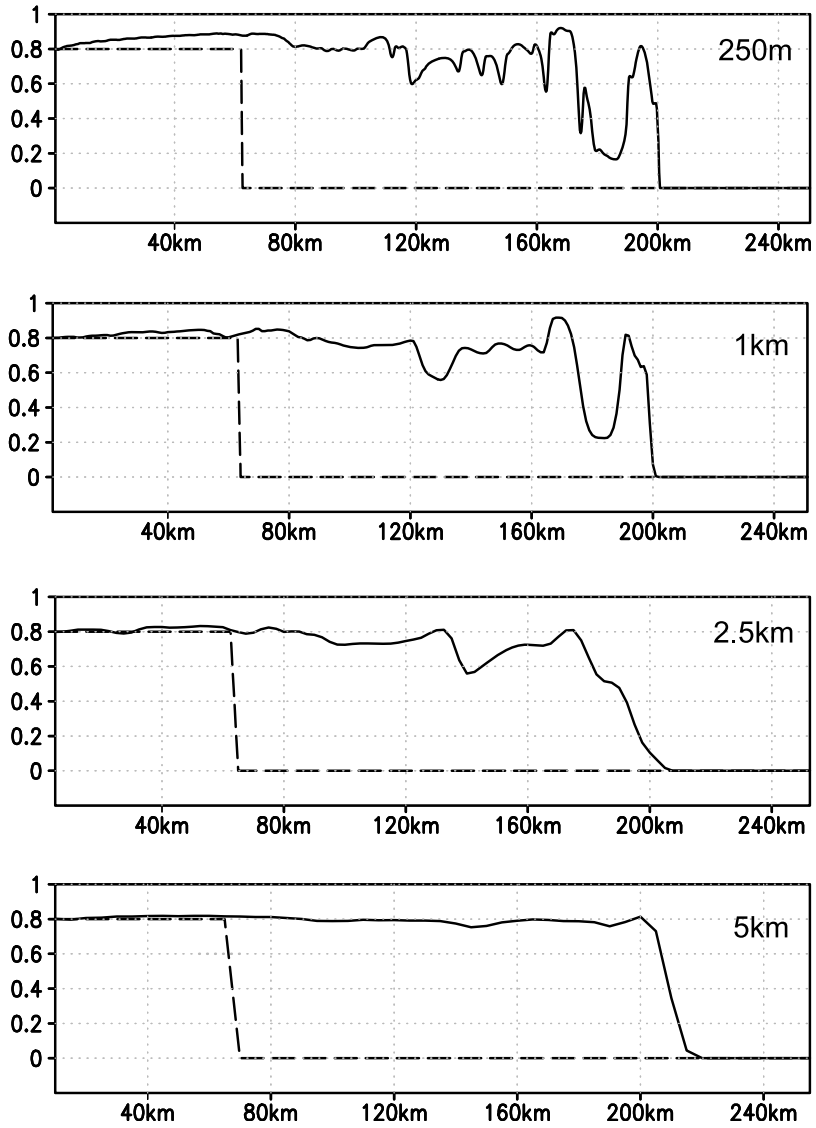


**Figure 8.** Ice concentration $A$ in Expt. Seven at day#15, for the indicated horizontal grid sizes: 250 m, 1 km, 2.5 km, and 5 km.

simple case when the ice concentration $A$ changes only as a result of ocean convergence and divergence:

$$\frac{\partial A'}{\partial t} = -\overline{A}\frac{\partial u_i'}{\partial x} \tag{33}$$

$$A = A' + \overline{A} \tag{34}$$

$$u_i = u_i' + \overline{u}_i \tag{35}$$

[43] Prime and bar are perturbation and mean quantities, respectively. A more general case with a steady background flow can also be included without affecting the result. Note that $u_i'$ and $A'$ have the same wavelength. The $u_i'$ is described by equation (1), in which sea surface tilt force and the Coriolis force are neglected. Since the ice in this study is mostly in free drift, the internal stress is also negligible, and equation (1) is simplified to:

$$\frac{\partial \mathbf{u}_i'}{\partial t} - jf\mathbf{u}_i' = \alpha(\mathbf{u}_w' - \mathbf{u}_i') \tag{36}$$

[44] Bold symbols denote the complex notation $\mathbf{u}_i' = u_i' + jv_i'$, $\mathbf{u}_w' = u_w' + jv_w'$, and the ice-water stress (equation (3)) is linearized with $\alpha = \rho_w C_{Diw}\Delta u/\rho_i h$, where $\Delta u = |\mathbf{u}_w - \mathbf{u}_i|$ is a scale for the ice-water relative velocity. Here, $\mathbf{u}_w$ is calculated from equations (15) and (16) using the normal-mode solution equation (27):

$$\mathbf{u}_w = \frac{g a_n \Delta T \kappa^2}{(\kappa u_{edge})^2 - f^2}\exp(j\kappa\zeta) \tag{37}$$

[45] The solution to equation (36) is

$$\mathbf{u}_i = C\exp(-\alpha + jf)t + \frac{\alpha \mathbf{u}_w}{\alpha + j(f + \kappa u_{edge})} \tag{38}$$

where $C$ is an arbitrary constant. The first term on the right-hand side is a damped inertial oscillatory term, and the second term represents the transfer of the lee-wave motion

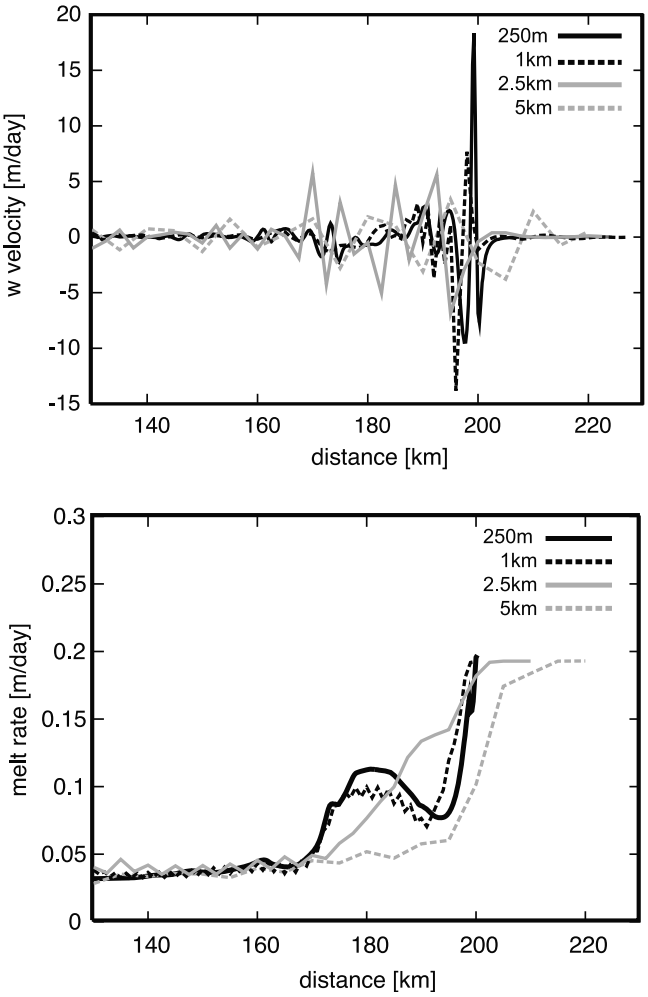


**Figure 9.** Day #15 of the simulation results from Expt. 7: (top) vertical velocity $w$ at z = −50 m and (bottom) melt rate. The region near the ice edge is zoomed in. The horizontal grid sizes are 250 m (solid), 1 km (dashed), 2.5 km (thin), 5 km (thin dashed).

to ice that creates ice bands. For large $t$, the first term is small and a "gain factor" $G$ may be defined:

$$G = \left|\frac{\mathbf{u}_i}{\mathbf{u}_w}\right| = \frac{1}{\sqrt{1 + \left(\frac{f + \kappa u_{edge}}{\alpha}\right)^2}} \tag{39}$$

[46] Figure 6 plots $G$ for various $\kappa$'s. Wavelengths shorter than 10 km are damped for typical $\Delta u$'s. This explains why the inter-band distance is larger than the lee-wavelength (Figure 1). The system is similar to the resistance-capacitance circuit that filters a high-frequency current (i.e., low-pass filter). Figure 7a shows the spectrum of $A$ and $w$ for Expt. 1, while Figure 7b shows the same for the experiment in which $u_i = u_w$ and the momentum equation (36) for ice is not solved (Expt. 3). Since the filtering effect is removed, the spectrum peaks of $A$ and $w$ coincide in this experiment. In the strong-wind experiment (Expt. 2), short-scale variations in $A$ appear (Figure 3, right) because the strong wind produces larger velocity differences, which increases $\alpha$ and $G$ for short wavelengths.

## 4. Grid Size Effects

[47] As is shown in the earlier sections, the interaction of ice bands and lee waves has a scale of O(1 km), which may not be resolved in many general circulation models. We evaluate the grid-size dependence of the formation of lee waves and ice bands using different horizontal grid sizes, namely 1. 2.5, and 5 km. The vertical resolution and other model parameters are kept the same as in the standard experiment with grid size = 250 m (Expt. 0). Figure 8 shows the ice concentration $A$ after 15 days. The 1km case still shows ice bands, but the 2.5 km and 5 km cases do not. The associated vertical velocity $w$ is weaker and noisier as the grid becomes coarser (Figure 9, top). Therefore, since small-scale convergence and divergence are accompanied by horizontal and vertical shears, significant shears are also absent when using coarse grid sizes.

[48] The melt rate is determined by ice-ocean heat transfer (equation (7)) and the temperature difference between ice bottom and sea surface, and can therefore be underestimated because of the lack of shears and intense vertical motion when coarse grids are used. Figure 9 shows that melt rates with the 1 km and 250 m grid sizes show peaks behind ice edge (Figure 9, bottom), whereas those from the 2.5 km and 5 km grid sizes do not. With the 2.5 km and 5 km grid sizes, Figure 8 shows that ice edges go farther instead of developing secondary peak behind ice edge. These experiments show that small-scale processes at the ice edge significantly affect the melt rate and therefore the ice edge position. The impact of these small-scale processes on regional and global ice-ocean models in which grid sizes are generally larger than 5km should be more carefully evaluated.

## 5. Three-Dimensional Effects

[49] The solutions presented above are limited to a two-dimensional ($xz$) domain. In this section, we confirm that ice bands are also formed by wind-induced lee waves in a more realistic three-dimensional setting (Expt. 8). Figure 10 shows that, after 15 days, an ice band is seen behind the ice edge 120 km < $x$ < 140 km. When compared to the corresponding two-dimensional experiments in Figures 1a and 8 (second panel), we see that the ice band moves slower. This is because some of the wind energy is transferred in producing along-ice ($y$) as eddy kinetic energy. Except for this difference, the two solutions are similar. The three-dimensional experiment shows that the two-dimensional approximation is valid up to a time period of approximately 10~15 days after the wind is applied. Beyond this period, wave-like features along the ice edge appear, and may indicate the beginning of flow instability that can lead to formation of eddies. We noted previously (Figure 2) that the maximum $PV$ is immediately under the ice-edge because of both local downward $PV$-flux and $PV$-advection from farther behind the ice-edge. The resulting change in sign of $PV$-gradient across the ice-edge can favor flow instability. This is an interesting topic that deserves a further study in the future.

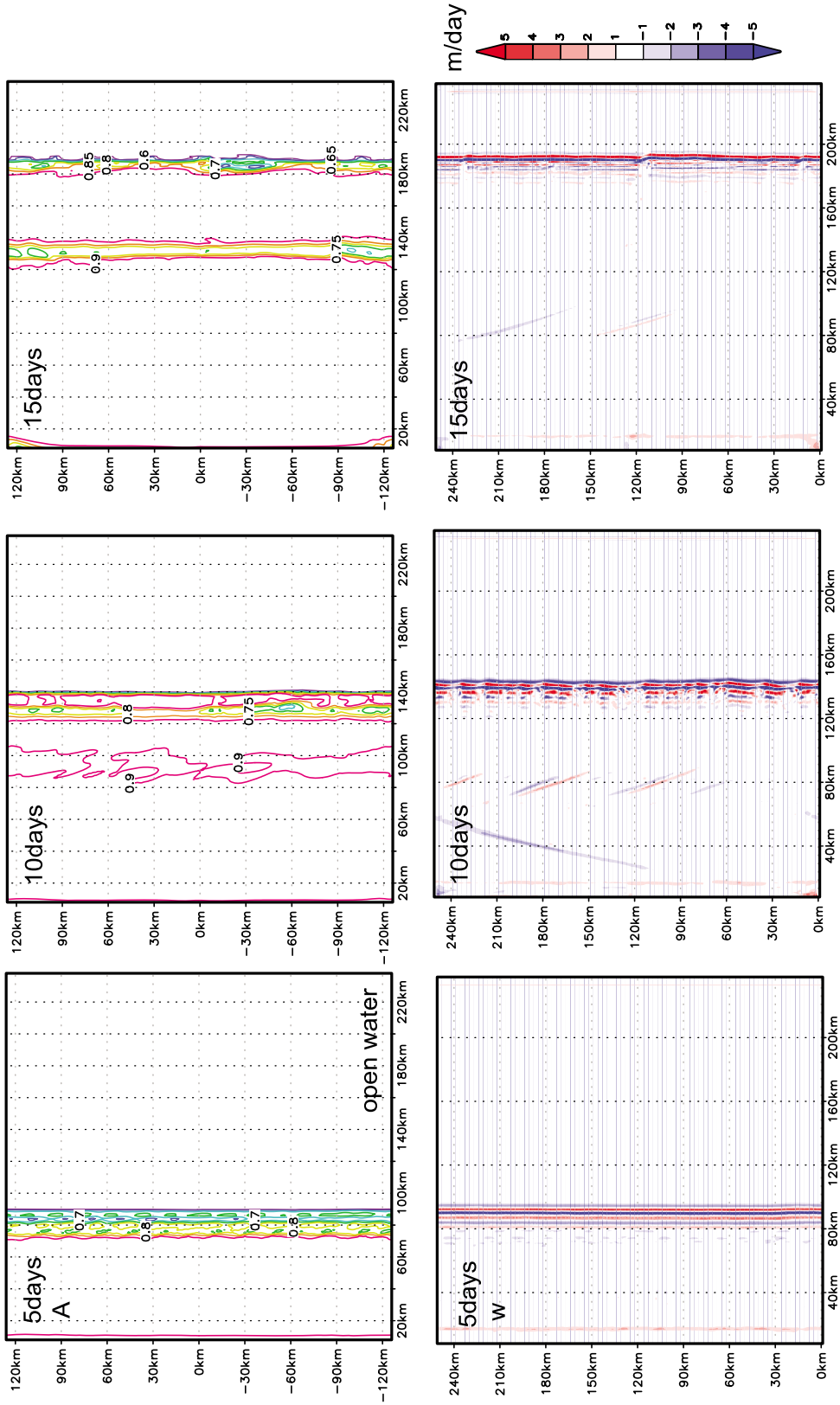


**Figure 10.** Expt. 8: three-dimensional model results at day#5, 10, and 15. (top) Ice concentration $A$. Ice edge advances from left to right. Contours are from 0.6 to 0.9 at 0.05 intervals. (bottom) Vertical velocity $w$ (m/day) at $z = -30$ m.

[50] Another future interest is to extend the study to the non-hydrostatic regime. *Marshall et al.* [1997] suggest that non-hydrostatic effects become significant when the non-hydrostatic parameter $N_h = h^2/(L^2 Ri) \gg O(1)$ or larger, where $h$ and $L$ are the depth and horizontal scales respectively and $Ri$ is the Richardson number. From the numerical experiment Expt. 0, near the ice-edge, $Ri \gg 1$, so that $N_h \ll 1$ for $h \gg 100$ m and lee-wavelength $\gg O(km)$, and the hydrostatic formulation used here to study lee-wind-generated ice bands is valid. However, the fine grid size of 250 m used here (and finer grid) may allow internal waves with wavelength comparable to the water depth (300 m) to develop in a non-hydrostatic model. It is possible then that the surface momentum flux can induce internal waves at the shallow pycnocline below the ice (i.e., dead water). How the present solution may be modified under these conditions is also an interesting future research topic.

## 6. Summary

[51] This paper examines the generation mechanism of ice bands as a coupled response to wind with lee waves under the hydrostatic approximation.

[52] Up-ice wind produces super-critical conditions for an ice edge moving faster than the lower-mode baroclinic phase velocity, and lee-waves are produced behind the ice edge. Ice bands are produced by the corresponding convergence and divergence. The associated vertical motions have speed of the order of 10 m/day, and extend to the bottom (300 m).

[53] Secondary lee waves are generated behind wedges of ice concentration because of the sharp variation of the corresponding sea surface stress. The flow reverts to sub-critical farther behind the ice edge where wave-like motions decay.

[54] Numerical experiments show that the inter-band distance is larger than the lee-wavelengths. We show that this is due to the smoothing effect of the ice-ocean stress.

[55] Ice-band formation and the associated strong vertical velocity are not resolved with horizontal grid sizes coarser than 1 km. We show that, when lee waves are resolved, the corresponding strong vertical motions and shears can mix and upwell deeper, warmer water to the surface and can accelerate melting. Sub-grid processes at the ice edge are therefore potentially significant contributors to melting and deep vertical mixing and melting. These mixing, upwelling and melting processes will not be adequately simulated in regional and global models in which horizontal grid sizes are typically larger than 5 km.

[56] **Acknowledgments.** A.F. was supported by the grant-in-aid for the Japan Society for Promotion of Science (20•9767), and L.Y.O. by NOAA's Office of Climate Programs, award NA17RJ2612. Some calculations were conducted at GFDL/NOAA.

## References

Geisler, J. E. (1970), Linear theory of the response of a two-layer ocean to a moving hurricane, *Geophys. Fluid Dyn.*, *1*, 249–272, doi:10.1080/03091927009365774.

Gill, A. E. (1982), *Atmosphere-Ocean Dynamics*, 662 pp., Academic, San Diego, Calif.

Häkkinen, S. (1986), Ice banding as a response of the coupled ice-ocean system to temporally varying winds, *J. Geophys. Res.*, *91*(C4), 5047–5053, doi:10.1029/JC091iC04p05047.

Hunke, E. C., and J. K. Dukowicz (1997), An elastic-viscous-plastic model for sea ice dynamics, *J. Phys. Oceanogr.*, *27*, 1849–1867, doi:10.1175/1520-0485(1997)027<1849:AEVPMF>2.0.CO;2.

Ishida, K., and K. I. Ohshima (2009), Ice-band characteristics of the Antarctic seasonal ice zone observed using MOS MESSR images, *Atmos. Ocean*, *47*(3), 169–183, doi:10.3137/OC300.2009.

Johannessen, O. M., J. A. Johannessen, J. Morison, B. A. Farrelly, and E. A. S. Svendsen (1983), Oceanographic conditions in the marginal ice zone north of Svalbard in early fall with an emphasis on mesoscale processes, *J. Geophys. Res.*, *88*(C5), 2755–2769, doi:10.1029/JC088iC05p02755.

Johannessen, O. M., W. J. Campbell, R. Shuchman, S. Sandven, and P. Gloersen (1992), Microwave study programs of air-ice-ocean interactive processes in the seasonal ice zone of the Greenland and Barents Seas, in *Microwave Remote Sensing of Sea Ice*, *Geophys. Monogr. Ser.*, vol. 68, edited by F. Carsey, chap. 13, pp. 261–289, AGU, Washington, D. C.

Marshall, J., C. Hill, L. Perelman, and A. Adcroft (1997), Hydrostatic, quasi-hydrostatic, and nonhydrostatic ocean modeling, *J. Geophys. Res.*, *102*(C3), 5733–5752, doi:10.1029/96JC02776.

McPhee, M. G., J. H. Morison, and F. Nilsen (2008), Revisiting heat and salt exchange at the ice-ocean interface: Ocean flux and modeling considerations, *J. Geophys. Res.*, *113*, C06014, doi:10.1029/2007JC004383.

Mellor, G., S. Häkkinen, T. Ezer, and R. Patchen (2002), A generalization of a sigma coordinate ocean model and an intercomparison of model vertical grids, in *Ocean Forecasting: Conceptual Basis and Applications*, edited by N. Pinardi and J. D. Woods, pp. 55–72, Springer, Berlin.

Millero, F. J. (1978), Freezing point of seawater, in *Eighth Report of the Joint Panel on Oceanographic Tables and Standards*, *UNESCO Tech. Pap. Mar. Sci.*, *28*, annex 6, UNESCO, Paris.

Muench, R. D., P. H. LeBlond, and L. E. Hachmeister (1983), On some possible interactions between internal waves and sea ice in the marginal ice zone, *J. Geophys. Res.*, *88*(C5), 2819–2826, doi:10.1029/JC088iC05p02819.

Rheem, C. K., H. Yamaguchi, and H. Kato (1997), Distributed mass/discrete floe model for pack ice rheology computation, *J. Mar. Sci. Technol.*, *2*(2), 101–121, doi:10.1007/BF02491524.

Sagawa, G. (2007), Development of ice dynamic model that takes account of floe collision and its validation in numerical sea ice forecast in the Sea of Okhotsk, Ph.D. diss., Univ. of Tokyo, Tokyo.

Sagawa, G., and H. Yamaguchi (2006), A Semi-Lagrangian sea ice model for high resolution simulation, paper presented at the 16th International Offshore and Polar Engineering Conference, Int. Soc. of Offshore and Pol. Engineers, San Francisco, California, 28 May to 2 June.

Sjøberg, B., and M. Mork (1985), Wind-induced stratified ocean response in the ice edge region: An analytical approach, *J. Geophys. Res.*, *90*(C4), 7273–7285, doi:10.1029/JC090iC04p07273.

Thomas, L. N. (2005), Destruction of potential vorticity by winds, *J. Phys. Oceanogr.*, *35*, 2457–2466, doi:10.1175/JPO2830.1.

Wadhams, P. (1983), A mechanism for the formation of ice edge bands, *J. Geophys. Res.*, *88*(C5), 2813–2818, doi:10.1029/JC088iC05p02813.

Wadhams, P. (2000), *Ice in the Ocean*, 351 pp., Gordon and Breach Sci. Publ., New York.

A. Fujisaki, Cooperative Institute for Limnology and Ecosystems Research, University of Michigan, 4840 S. State Rd., Ann Arbor, MI 48108, USA. (ayumif@umich.edu)

L.-Y. Oey, Atmospheric and Oceanic Science Program, Princeton University, Sayre Hall, Princeton, NJ 08544, USA. (lyo@princeton.edu)